effective diameter of a FLL, (2) the ratio of vessel-like pattern areas to the whole liver area within a MFI image, and (3) the average size of the vessel-like patterns. The average size of vessel-like patterns was determined by use of the vessel-like pattern and its skeleton images. Figure 7 shows an example of a skeleton image obtained from the vessel-like pattern image. In this method, we assumed that an approximate average size of a vessel-like pattern can be estimated by use of the ratio of the area of the skeleton image and the area of the vessel-like pattern image.

We also extracted three gray-level image features based on the MFI image at the early and the delayed phases, such as (1) the average pixel value without and with the segmented vessel-like patterns, (2) the standard deviation of pixel values without and with the segmented vessel-like patterns, and (3) two ratios of average pixel values for those in a FLL to an ALP, and for those in the central to the peripheral region of the FLL. The average pixel values were obtained from the whole and central/peripheral regions of a FLL, whereas the others were obtained only from the whole region of a FLL.

Moreover, in order to obtain additional image features related to hypoechoic regions, we segmented hypoechoic regions within a region of the FLL. In this computerized scheme, the Gaussian-filter technique was applied to gray-scale-inverted MFI images at the early and the delayed phases. Because the replenishment of the contrast agent (microbubble) was imaged on the MFI image, vessels were imaged partially at the early phase and then were imaged fully at the delayed phase. The minimum size of the hepatic artery which could be imaged on MFI was approximately 3.0 mm. In order to remove noise components with enhancement of the hepatic arteries in two phases of the MFI images, therefore, we determined the kernel sizes for the Gaussian-filter technique with 2.0 and 3.0 mm for the MFI images obtained at the early and the delayed phases, respectively. The pixel value of the thresholding hypoechoic region on the filtered image was determined empirically as 192, and used for both filter sizes and all 103 FLLs. In other words, the regions with 25% or less than 25% of peak pixel values were considered to be a hypoechoic region. Figure 9 shows an example of a segmented hypoechoic region at the early and the delayed phases and the MFI image at the delayed phase. By use of the information about the segmented hypoechoic regions, we extracted additional image features, such as (1) the number of hypoechoic regions within a FLL, (2) the ratio of the area of hypoechoic regions to the whole area of the FLL, (3) the difference in the average pixel values between the early and the delayed phases, and (4) the average change in pixel values per second in delayed-enhancement regions. We defined a delayed-enhancement region when the region was included in the segmented hypoechoic region at the early phase, but not in the delayed phase, as shown in Fig. 9.

Table I shows the total of 43 temporal and image features extracted initially in this computerized scheme.

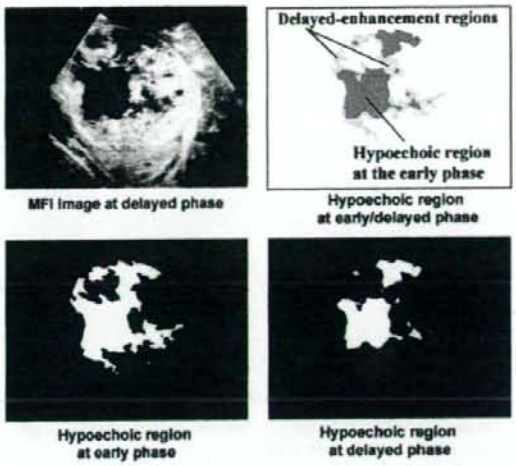

FIG. 9. Example of the original MFI image at the delayed phase and its segmented images for hypoechoic regions at the early and delayed phases. The difference in the regions between two images at two phases was defined as delayed-enhancement region.

II.D.5. Feature selection and application of a cascade of ANNs

In order to classify five types of FLLs, we employed a cascade of six ANNs. Figure 10 illustrates a cascade of six ANNs used in this CAD scheme.

The number of ANNs of six was determined with the number of types of FLLs of seven (i.e., three types of HCCs, hyper- and hypovascularity metastasis, and hyper- and hypovascularity hemangioma). The order of the six decisions (D1–D6) at each ANN was determined based on the diagnostic difficulties, which were described in Sec. II C.[17–19,23,28] The six decisions used in this study are shown as follows:

- D1: Does this lesion have hypoechoic regions (yes) or not (no)?
- D2: Is this lesion a hypovascularity hemangioma (yes) or a hypovascularity metastasis (no)?
- D3: Is this lesion a hypervascularity hemangioma (yes) or other (no)?
- D4: Is this lesion a poorly differentiated HCC (yes) or other (no)?
- D5: Is this lesion a well differentiated HCC (yes) or other (no)?
- D6: Is this lesion a moderately differentiated HCC (yes) or a hypervascularity metastasis (no)?

All decisions were determined by ANNs in terms of a two-alternative choice. In all of the six ANNs, we employed one hidden layer, one half of the number of input units as the number of hidden units, one output unit, 0.05 for the learning rate, and 0.30 for the slope of the sigmoid function. These parameters were determined based on our experimental knowledge gained in previous research.[38] The seven combinations of the number of input units and iterations (2 and 200, 3 and 200, 3 and 300, 4 and 300, 4 and 400, 5 and 300,

TABLE I. List of 43 temporal and image features obtained from the original and temporally averaged images with whole, central, and peripheral regions. Features were extracted from a contour provided by a physician (C), a series of images (S), at the early-phase image (E), and at the delayed image (D). Bold type and a subscript number indicate the selected 19 features and ANN numbers. [C, S, E, and D represent the image(s) for feature extraction, such as a contour image, a series of images, an image at the early and the delayed phase, respectively. Bold type and following subscript number indicate a feature selected and its series number in six ANNs.]

	Original images			Temporally averaged images		
	Whole	Central	Peripheral	Whole	Central	Peripheral
Temporal features						
Replenishment time (s)				$\mathbf{D_{3,5,6}}$		
Peak pixel value				S		
Slope factor (β)				S		
Morphologic features						
Effective diameter of FLL	$\mathbf{C_{1,4,5}}$					
Average size of vessel-like patterns				$\mathbf{D_2}$	D	$\mathbf{D_2}$
Area ratio of vessel-like patterns				$\mathbf{D_2}$	$\mathbf{D_2}$	D
Gray-level features						
Average pixel value with vessel-like patterns	E, D	E, $\mathbf{D_3}$	E, D	E, D	$\mathbf{E_6}$, D	$\mathbf{E_6}$, D
Average pixel value without vessel-like patterns				$\mathbf{D_3}$		
Standard deviation of pixel value with vessel-like patterns				E, $\mathbf{D_4}$		
Standard deviation of pixel value without vessel-like patterns				$\mathbf{D_5}$		
Average pixel value ratio (FFL/AHP)	E, D			$\mathbf{E_6}$, D		
Average pixel value ratio (central/peripheral)				E, $\mathbf{D_6}$		
Features for hypoechoic region						
Average pixel value				E, D		
No. of hypoechoic regions				E, D		
Area ratio of hypoechoic region				E, D	$\mathbf{D_{1,4}}$	
Difference in pixel value (delay-early)				E/D		
Change in pixel value (delay-early)/s				$\mathbf{E/D_4}$		

and 5 and 400) were tested for determining the appropriate parameters for each ANN. The maximum number of input unit was determined by five because the limited number of cases used in this study. The numbers of iterations corresponding to the number of input units were selected based on our experimental knowledge.[38]

In order to select appropriate combinations of temporal and image features for each of the six ANNs, we used a stepwise method.[40] Although a conventional stepwise regression applies a sequence of F tests for determining the necessity and sufficiency of temporally selected features by use of their p values, we employed an ANN and the diagnostic accuracy estimated by the ANN instead of the F test and its p value. In this stepwise procedure, the feature selection was started by selection of the best candidate pair of feature combinations which had the maximum diagnostic accuracy in the training ANN with a selected number of iterations, as described above. In the forwarding selection of the stepwise after the best candidate pair of feature combinations had been selected, the remaining features were tried out one by one and considered as the best candidate combination if the diagnostic accuracy of this combination was greater than that with the last best candidate combination. In the backward selection, which involves starting with all features in the best candidate combination and testing them one by one with an

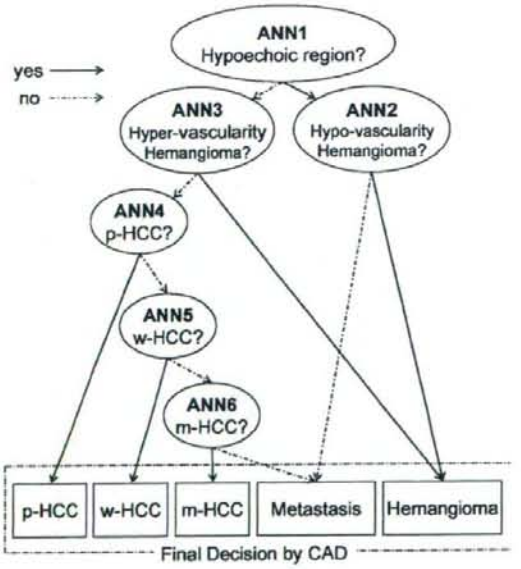

FIG. 10. Illustration of the cascade of six ANNs used in this study. Six decisions in which alternative choices for specific groups of FLLs were determined by single ALL, leading a final diagnostic decision for five liver diseases.

TABLE II. Number of FLLs and classification accuracies obtained by CAD for well differentiated HCCs, moderately differentiated HCCs, and poorly differentiated HCCs, metastases, and hemangiomas.

Type of disease		No. of lesions	Classification with CAD				
			HCC				
			Well	Moderate	Poor	Metastasis	Hemangioma
HCC	Well	24	19 (79.2%)	1 (4.2%)	2 (8.3%)	2 (8.3%)	0 (0.0%)
	Moderate	28	5 (17.9%)	14 (50.0%)	4 (14.3%)	3 (10.7%)	2 (7.1%)
	Poor	9	1 (11.1%)	0 (0.0%)	7 (77.8%)	1 (11.1%)	0 (0.0%)
Metastasis		26	2 (7.7%)	1 (3.8%)	0 (0.0%)	23 (88.5%)	0 (0.0%)
Hemangioma		16	0 (0.0%)	0 (0.0%)	0 (0.0%)	1 (6.3%)	15 (93.8%)

ANN and estimating the diagnostic accuracy, deleting any if the diagnostic accuracy for the combination without a tested feature was not changed from that of the best candidate combination. Then, the forward and backward selections were repeated until the number of selected features reaches the preset maximum number of features, and the maximum diagnostic accuracy was not changed.

Finally, we selected the number of features (input units) and iterations, such as 2 and 200 for D1, 4 and 300 for D2, 3 and 300 for D3, 4 and 300 for D4, 4 and 400 for D5, and 5 and 400 for D6, and a total of 16 image features for the six ANNs. Table I also shows selected features of each ANN.

The six ANNs were trained and tested with a leave-one-lesion-out method independently by use of selected features and the number of iterations. In the leave-one-lesion-out test method used in this study, because the number of lesions subjected to training of each of the six ANNs were sometimes small and imbalanced, such as 81versus 22 for D1, 11 versus 11 for D2, 76 versus 5 for D3, 67 versus 9 for D4, 43 versus 24 for D5, and 28 versus 15 for D6, the numbers of positive and negative lesions in each of the six ANNs was matched to one another by duplicating of input data sets in order to reduce a bias due to the imbalance of the numbers of positive and negative lesions. The target value during the ANN for positive lesions (i.e., the specific group with answer "yes" to each decision) was 0.95, and 0.05 for negative (i.e., the specific group with answer "no" to each decision) lesions.

In order to use ANNs for making a two-alternative choice (i.e., yes or no) in each decision in the cascade of six ANNs, we used a fixed threshold value of 0.50 for distinguishing decisions made by the ANN output (i.e., 0.50 or more is yes, all others are no). The correct classification of the CAD scheme for three types of HCCs was determined when the final branch of a cascade of six ANNs which was led by a number of decisions agreed with its "gold standard." Metastasis and hemangioma cases were considered as correctly classified by the CAD when its final branch was correctly selected from either FLLs without or those with hyperechoic regions. The classification accuracies for each type of FLL and also for all 103 FLLs were determined with percentages (%) of correctly classified cases among a total number of cases. Please note that we did not monitor the classification accuracies during training and testing of the six ANNs in the cascade.

III. RESULTS

The computer performance in terms of the number of FLLs correctly classified and the classification accuracies (%) in each of the six ANNs were 102 of 103 (99.3%) for D1, 21 of 22 (95.5%) for D2, 79 of 81 (97.5%) for D3, 69 of 76 (90.8%) for D4, 56 of 67 (83.6%) for D5, and 37 of 43 (86.1%) for D6.

Table II shows the performance of the computerized scheme for the classification of five types of FLLs (*w*-HCCs, *m*-HCCs, *p*-HCCs, metastases, and hemangiomas). The classification accuracies for the 103 FLLs were 88.5% for metastasis, 93.8% for hemangioma, 79.2% for *w*-HCC, 50.0% for *m*-HCC, and 77.8% for *p*-HCC. When the classification was done for three types of FLLs (HCCs, metastasis, and hemangioma), the classification accuracies for all HCCs was 86.9%. The average classification accuracies for three and five types of FLLs were 88.3% and 75.7%, respectively. Figure 11 shows examples of MFI images for each of the five diseases which were classified correctly by the CAD.

As shown in Table II, 12 FLLs, which were incorrectly classified into three types of liver diseases by the CAD, consisted of eight HCCs, three metastases, and one hemangioma. The CAD incorrectly classified eight HCCs as six metastases and two hemangiomas, three metastases as three HCCs, and one hemangioma as one metastasis. Therefore, the classification accuracies for malignant (HCCs and metastases) and for benign (hemangiomas) lesions were 97.7% and 93.8%, respectively.

IV. DISCUSSION

In this CAD scheme, we employed a cascade of six independent ANNs. Because each ANN was designed specially for each decision by selection of appropriate image features, the majority of FLLs which had any of the typical patterns were classified correctly by the computer. In order to represent vascular patterns and temporal characteristics for all types of FLLs as close as possible to physicians' diagnostic

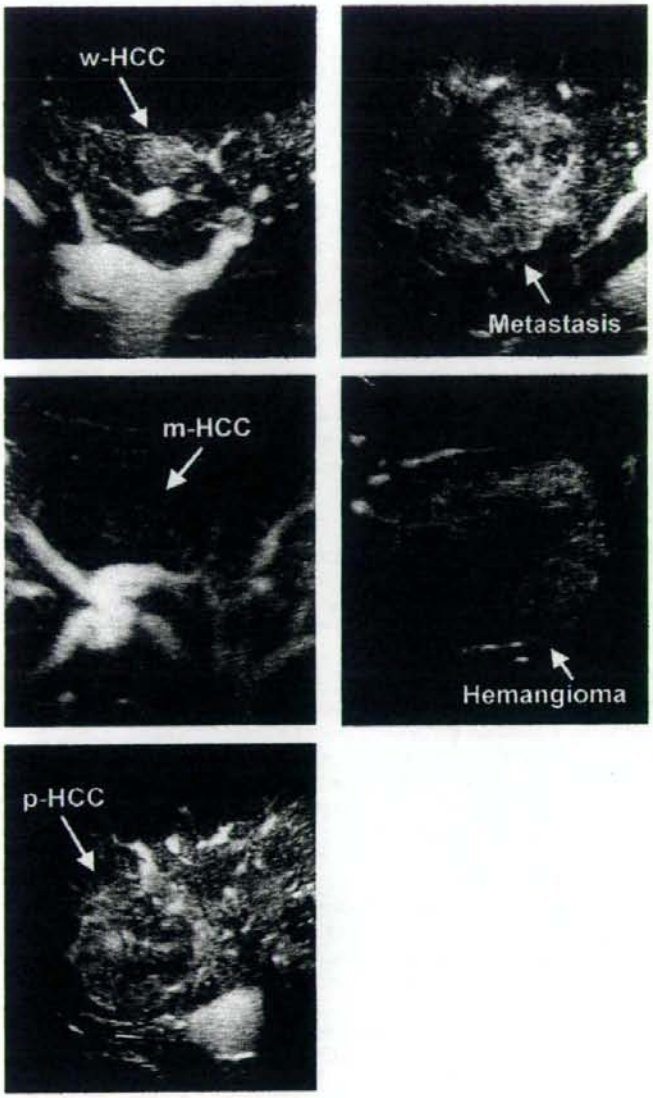

FIG. 11. Examples of correctly classified cases. (a) *w*-HCC showed relatively uniform and isoechoic replenishment patterns, and the size was relatively small (15.9 mm, pixel size: 0.29 mm). (b) *m*-HCC showed a relatively isoechoic replenishment pattern, but the size was large (23.4 mm, pixel size: 0.17 mm), and the replenishment pattern within a lesion was not uniform. (c) *p*-HCC had a relatively large size (20.1 mm, pixel size: 0.34 mm) and showed branched tumor vessels within a lesion. (d) Metastasis (hypovascularity type) had a large size (65.6 mm, pixel size: 0.29 mm) and showed a hypoechoic region at the center of the lesion at the delayed phase. And (e) hemangioma (hypovascularity type) had a relatively large size (56.6 mm, pixel size: 0.26 mm) and was replenished very slowly with centripetal progression.

knowledge, we initially extracted 43 temporal and image features. However, only 16 features, including one temporal feature, five morphologic features, eight gray-level features, and two features for hypoechoic regions were selected for all ANNs (note that the maximum number of selected features for a single ANN was five). For example, in the first ANN for distinguishing FLLs with from those without hypoechoic regions, an image feature of the area ratio of the hypoechoic regions to that within a FLL was dominant among the selected two features. For example, 78 of 81 FLLs (61 HCCs and 15 hypervascularity metastases, and five hypervascularity hemangiomas) had no obvious hypoechoic regions at their delayed phases. For the second ANN, in a comparison between the hypovascularity hemangiomas and the hypovascularity metastases, tumor vessels in the central region of the hypovascularity hemangiomas were likely not to be enhanced within an acquisition time (range from 4.1 to 23.1 s) of the MFI. Thus, morphologic features related to vessel-like patterns in the central and peripheral regions were effective for distinguishing them. For distinguishing hypervascularity hemangiomas in the third ANN, a temporal feature of the estimated replenishment time at the delayed phase was effective because the estimated replenishment time for hemangioma was likely to be long compared with that for the other

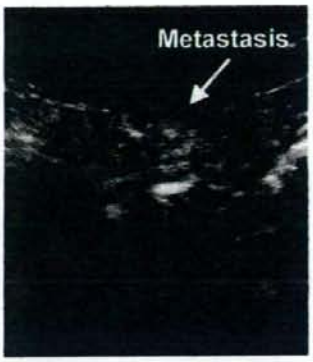

FIG. 12. Example of the CAD output for a FLL (hypervascularity metastasis) which was incorrectly classified as *m*-HCC, because the size of this lesion was relatively large (25.1 mm, pixel size: 0.24 mm), and the echogenicity of this metastasis was isoechoic to those in ALP regions.

types of liver diseases. The *p*-HCCs were likely to be large and to indicate a heterogeneous enhancement pattern due to thick tumor vessels compared with *w*-HCCs, *m*-HCCs, and hypervascularity metastases. Therefore, the effective diameter and the standard deviation of pixel values in a FLL with vessel-like pattern regions were effective in the fourth ANN. For distinguishing *w*-HCCs from *m*-HCCs and hypervascularity metastases, the standard deviation of pixel values in a FLL without vessel-like pattern regions and the estimated replenishment time at the delayed phase was effective because *w*-HCCs were likely to be enhanced uniformly and slowly compared with those with *m*-HCCs and with hypervascularity metastases. It is well known that the distinction between *m*-HCCs and hypervascularity metastases was very difficult for physicians.[11] However, as shown in Fig. 2, some *m*-HCCs were likely to be enhanced with centrifugal or centripetal patterns; therefore, we selected the ratio of the average pixel values in the central region of a FLL to that in the peripheral region. Figure 12 shows one example of a metastasis case which was classified incorrectly as *w*-HCC. As shown in Fig. 12, it is very difficult to distinguish hypervascularity metastases from HCCs because they show identical vascularity patterns in the arterial phase.[24]

The performance of our CAD scheme for the classification of FLLs could be considered as comparable to those reported by Wilson and Burns.[23] Although their performance was not the results of the CAD, their algorithm used the subjective assessment of physicians for information on portal venous enhancement in the distinction between benign and malignant FLLs and indicated a very high classification accuracy (i.e., 92% for benign and 93% for malignant FLLs),[22] which was evaluated by use of a resubstitution method.

In this study, we used MFI images which were selected from either the arterial or the portal venous phase of contrast-enhancement ultrasonography because the appropriate enhancement phase for distinguishing FLLs depended on the type of disease as well as the physicians' judgment. In addition, locations and contours of FLLs were determined by only one physician in this study. Although the margin of each FLL was drawn concisely, as shown in Figs. 7, 8, and 10, and we did not use the shape of FLLs (such as circularity and irregularity) for the image feature analysis, there would be some variations in the performance of the CAD scheme due to the physician dependence. Furthermore, the quality of the MFI images depended on the patients' condition. Therefore, as is well-known, a potential limitation for all ultrasonographic studies is that the image acquisition of the MFI is operator dependent.

Replenishment vascularity patterns in the MFI with second-generation perfluorocarbon agents were slightly different from those in the arterial and portal vein phases in pulse-inversion imaging with the second-generation air-based contrast agent in terms of continuous imaging of inflow high signals. However, most of the vascularity patterns for FLLs were common to both imaging methods, so that we could take into account some specific vascularity patterns in our computerized scheme.

In this study, the gold standard for evaluating the computerized scheme was determined by pathology. However, because we used the MFI images obtained from only one section, mixtures of two or three histologic differentiation types in a FLL were not taken into account in our evaluation. In addition, because specimens for histopathologic diagnosis of the degree of differentiation of HCCs were obtained by use of a fine-needle biopsy, the specimen allowed us to evaluate only a small part of the HCC lesion. Therefore, the computer performance for the classification between three differentiated types of HCCs was potentially underestimated.

There are several limitations to this CAD study. On the one hand, the number of cases used in this study was relatively small, and only five types of liver diseases were included in the database. For example, we did not include FNH because the number of FNH cases was very small. However, we believe that the computerized scheme with MFI can be modified for classifying six types of liver diseases, including FNH cases when the number of FNH cases is increased because the image characteristics of FNH in contrast-enhanced ultrasonography also have been studied thoroughly.[10,17,23]

Other limitations were that feature selection and parameter settings were determined empirically and by use of a stepwise method for each ANN, even though six ANNs in the cascade were trained and tested by a leave-one-lesion-out method by use of selected features, and the final result obtained from the cascade of six ANNs was not monitored during the training and testing of six ANNs. This feature selection method depended on the database used, and thus, there could be some bias in the evaluation of results.[41] However, a number of features were reasonably selected in each ANN in terms of the agreement with physicians' knowledge, and thus, physicians' confidence in the use of the CAD scheme would be improved. In addition, a number of parameters used in this CAD scheme were determined empirically or based on our experimental knowledge. For justifying the determination of these parameters, further systematic study with a large-scale image database would be necessary in the future.

V. CONCLUSION

We developed a computerized scheme for the classification of focal liver lesions by use of MFI of contrast-enhanced ultrasonography. The performance of this CAD scheme has the potential to improve the diagnostic accuracy of the histologic characteristics of HCCs and other liver diseases.

ACKNOWLEDGMENTS

The authors are grateful to Elisabeth Lanzl for improving the manuscript. This work is supported by USPHS Grant Nos. CA62625 and CA98119 and by the Toshiba Corporation. CAD technologies developed in the Kurt Rossmann Laboratories have been licensed to companies including R2 Technology, Deus Technologies, Riverain Medical Group, Mitsubishi Space Software Co., Median Technologies, General Electric Corporation, and Toshiba Corporation. It is the policy of The University of Chicago that investigators disclose publicly actual or potential significant financial interests that may appear to affect research activities or that may benefit from research activities.

[a]Present address: Kurt Rossmann Laboratories for Radiologic Image Research, Department of Radiology, The University of Chicago, 5841 S. Maryland Ave., MC 2026, Chicago, IL 60637. Telephone: (773) 834-5091; Fax: (773)702-0371. Electronic mail: junji@uchicago.edu

[1]A. Laghi, R. Iannaccone, P. Rossi, I. Carbone, R. Ferrari, F. Mangiapane, I. Nofroni, and R. Passariello, "Hepatocellular carcinoma: detection with triple-phase multi-detector row helical CT in patients with chronic hepatitis," Radiology **226**, 543–549 (2003).

[2]D. R. Martin, and R. C. Semelka, "Imaging of benign and malignant focal liver lesions," Magn. Reson. Imaging Clin. N. Am. **9**, 785–802 (2001).

[3]S. M. Hussain, R. C. Semelka, and D. G. Mitchell, "MR imaging of hepatocellular carcinoma," Magn. Reson. Imaging Clin. N. Am. **10**, 31–52 (2002).

[4]Y. Yamashita, Y. Hatanaka, H. Yamamoto, A. Arakawa, T. Matsukawa, T. Miyazaki, and M. Takahashi, "Differential diagnosis of focal liver lesions: role of spin-echo and contrast-enhanced dynamic MR imaging," Radiology **193**, 59–65 (1994).

[5]K. Wernecke, E. Rummeny, G. Bongartz, P. Vassallo, D. Kivelitz, W. Wiesmann, P. E. Peters, B. Reers, M. Reiser, and W. Pircher, "Detection of hepatic masses in patients with carcinoma: Comparative sensitivities of sonography, CT, and MR imaging," AJR Am. J. Roentgenol. **157**, 731–739 (1991).

[6]P. N. Burns, S. R. Wilson, and D. H. Simpson, "Pulse inversion imaging of liver blood flow: Improved method for characterizing focal masses with microbubble contrast," Invest. Radiol. **35**, 58–71 (2000).

[7]P. N. Burns, "Harmonic imaging with ultrasound contrast agents," Clin. Radiol. **51**, 50–55 (1996).

[8]P. N. Burns and S. R. Wilson, "Focal liver masses: Enhancement patterns on contrast-enhanced images–concordance of US scans with CT scans and MR images," Radiology **242**, 162–174 (2007).

[9]E. Quaia, F. Calliada, M. Bertolotto, S. Rossi, L. Garioni, L. Rosa, and R. Pozzi-Mucelli, "Characterization of focal liver lesions with contrast-specific US modes and a sulfur hexafluoride-filled microbubble contrast agent: Diagnostic performance and confidence," Radiology **232**, 420–430 (2004).

[10]M. J. Dill-Macky, P. N. Burns, K. Khalili, and S. R. Wilson, "Focal hepatic masses: Enhancement patterns with SH U 508A and pulse-inversion US," Radiology **222**, 95–102 (2002).

[11]T. Albrecht, M. J. Blomley, P. N. Burns, S. Wilson, C. J. Harvey, E. Leen, M. Claudon, F. Calliada, J. M. Correas, M. Lafortune, R. Campani, C. W. Hoffmann, D. O. Cosgrove, and F. Lefevre, "Improved detection of hepatic metastases with pulse-inversion US during the liver-specific phase of SHU 508A: Multicenter study," Radiology **227**, 361–370 (2003).

[12]M. Bertolotto, L. Dalla Palma, E. Quaia, and M. Locatelli, "Characterization of unifocal liver lesions with pulse inversion harmonic imaging after Levovist injection: Preliminary results," Eur. Radiol. **10**, 1369–1376 (2000).

[13]M. J. Blomley, T. Albrecht, D. O. Cosgrove, N. Patel, V. Jayaram, J. Butler-Barnes, R. J. Eckersley, A. Bauer, and R. Schlief, "Improved imaging of liver metastases with stimulated acoustic emission in the late phase of enhancement with the US contrast agent SH U 508A: Early experience," Radiology **210**, 409–416 (1999).

[14]M. Brannigan, P. N. Burns, and S. R. Wilson, "Blood flow patterns in focal liver lesions at microbubble-enhanced US," Radiographics **24**, 921–935 (2004).

[15]B. I. Choi, T. K. Kim, J. K. Han, A. Y. Kim, C. K. Seong, and S. J. Park, "Vascularity of hepatocellular carcinoma: assessment with contrast-enhanced second-harmonic versus conventional power Doppler US," Radiology **214**, 381–386 (2000).

[16]M. Golli, D. Mathieu, M. C. Anglade, D. Cherqui, N. Vasile, and A. Rahmouni, "Focal nodular hyperplasia of the liver: Value of color Doppler US in association with MR imaging," Radiology **187**, 113–117 (1993).

[17]C. Huang-Wei, A. Bleuzen, P. Bourlier, J. Roumy, A. Bouakaz, L. Pourcelot, and F. Tranquart, "Differential diagnosis of focal nodular hyperplasia with quantitative parametric analysis in contrast-enhanced sonography," Invest. Radiol. **41**, 363–368 (2006).

[18]S. H. Kim, J. M. Lee, J. Y. Lee, J. K. Han, S. K. An, C. J. Han, K. H. Lee, S. S. Hwang, and B. I. Choi, "Value of contrast-enhanced sonography for the characterization of focal hepatic lesions in patients with diffuse liver disease: receiver operating characteristic analysis," AJR Am. J. Roentgenol. **184**, 1077–1084 (2005).

[19]M. Omata, "Can contrast-enhanced sonography be used to characterize focal hepatic lesions in patients with liver disease?" Nat. Clin. Pract. Gastroenterol. Hepatol. **2**, 452–453 (2005).

[20]E. Quaia, M. Bertolotto, and L. Dalla Palma, "Characterization of liver hemangiomas with pulse inversion harmonic imaging," Eur. Radiol. **12**, 537–544 (2002).

[21]P. Ricci, A. Laghi, V. Cantisani, P. Paolantonio, S. Pacella, E. Pagliara, F. Arduini, V. Pasqualini, F. Trippa, M. Filpo, and R. Passariello, "Contrast-enhanced sonography with SonoVue: Enhancement patterns of benign focal liver lesions and correlation with dynamic gadobenate dimeglumine-enhanced MRI," AJR Am. J. Roentgenol. **184**, 821–827 (2005).

[22]S. R. Wilson and P. N. Burns, "Liver mass evaluation with ultrasound: The impact of microbubble contrast agents and pulse inversion imaging," Semin. Liver Dis. **21**, 147–159 (2001).

[23]S. R. Wilson and P. N. Burns, "An algorithm for the diagnosis of focal liver masses using microbubble contrast-enhanced pulse-inversion sonography," AJR Am. J. Roentgenol. **186**, 1401–1412 (2006).

[24]S. R. Wilson, P. N. Burns, D. Muradali, J. A. Wilson, and X. Lai, "Harmonic hepatic US with microbubble contrast agent: initial experience showing improved characterization of hemangioma, hepatocellular carcinoma, and metastasis," Radiology **215**, 153–161 (2000).

[25]C. Yucel, H. Ozdemir, S. Gurel, S. Ozer, and M. Arac, "Detection and differential diagnosis of hepatic masses using pulse inversion harmonic imaging during the liver-specific late phase of contrast enhancement with Levovist," J. Clin. Ultrasound **30**, 203–212 (2002).

[26]A. M. Di Bisceglie, "Hepatitis C and hepatocellular carcinoma," Hepatology **26**, 34S–38S (1997).

[27]H. B. El-Serag and A. C. Mason, "Rising incidence of hepatocellular carcinoma in the United States," N. Engl. J. Med. **340**, 745–750 (1999).

[28]B. Sun, S. Zhang, D. Zhang, J. Du, H. Guo, X. Zhao, W. Zhang, and X. Hao, "Vasculogenic mimicry is associated with high tumor grade, invasion and metastasis, and short survival in patients with hepatocellular carcinoma," Oncol. Rep. **16**, 693–698 (2006).

[29]K. Doi, "Current status and future potential of computer-aided diagnosis in medical imaging," Br. J. Radiol. **78**, S3–S19 (2005).

[30]K. Doi, "Computer-aided diagnosis in medical imaging: Historical review, current status and future potential," Comput. Med. Imaging Graph. **31**, 198–211 (2007).

[31]M. Gletsos, S. G. Mougiakakou, G. K. Matsopoulos, K. S. Nikita, A. S. Nikita, and D. Kelekis, "A computer-aided diagnostic system to characterize CT focal liver lesions: Design and optimization of a neural network classifier," IEEE Trans. Inf. Technol. Biomed. **7**, 153–162 (2003).

[32]Y. L. Huang, J. H. Chen, and W. C. Shen, "Diagnosis of hepatic tumors with texture analysis in nonenhanced computed tomography images," Acad. Radiol. **13**, 713–720 (2006).

[33]R. Metoki, F. Moriyasu, N. Kamiyama, K. Sugimoto, H. Iijima, H. X. Xu, T. Aoki, Y. Miyata, K. Yamamoto, K. Kudo, M. Shimizu, and M. Yamada, "Quantification of hepatic parenchymal blood flow by contrast ultrasonography with flash-replenishment imaging," Ultrasound Med. Biol. **32**, 1459–1466 (2006).
[34]K. Wei, A. R. Jayaweera, S. Firoozan, A. Linka, D. M. Skyba, and S. Kaul, "Quantification of myocardial blood flow with ultrasound-induced destruction of microbubbles administered as a constant venous infusion," Circulation **97**, 473–483 (1998).
[35]P. Burns, "Imaging methodology for new contrast agents, basic and clinical aspects," Poceedings of the 4th International Symposium On Ultrasound Contrast Imaging, 2002, pp. 28–30.
[36]J. Powers, S. Jensen, and E. Al, "Microvascular imaging of the breast," Proceedings of the 8th European Symposium on Ultrasound Contrast Imaging, 2003, p. 8.
[37]T. K. Kim, B. I. Choi, J. K. Han, H. S. Hong, S. H. Park, and S. G. Moon, "Hepatic tumors: Contrast agent-enhancement patterns with pulse-inversion harmonic US," Radiology **216**, 411–417 (2000).
[38]J. Shiraishi, Q. Li, K. Suzuki, R. Engelmann, and K. Doi, "Computer-aided diagnostic scheme for the detection of lung nodules on chest radiographs: Localized search method based on anatomical classification," Med. Phys. **33**, 2642–2653 (2006).
[39]M. L. Giger, K. Doi, and H. MacMahon, "Image feature analysis and computer-aided diagnosis in digital radiography. 3. Automated detection of nodules in peripheral lung fields," Med. Phys. **15**, 158–166 (1988).
[40]R. R. Hocking, "The analysis and selection of variables in linear regression," Biometrics **32**, 1–49 (1976).
[41]Q. Li and K. Doi, "Comparison of typical evaluation methods for computer-aided diagnostic schemes: Monte Carlo simulation study," Med. Phys. **34**, 871–876 (2007).

Hepatology Research 2008; 38: 790–799 doi: 10.1111/j.1872-034X.2008.00331.x

Original Article

Analysis of morphological vascular changes of hepatocellular carcinoma by microflow imaging using contrast-enhanced sonography

Katsutoshi Sugimoto,[1] Fuminori Moriyasu,[1] Naohisa Kamiyama,[2] Ryo Metoki,[1] Masahiko Yamada,[1] Yasuharu Imai[1] and Hiroko Iijima[3]

[1]Department of Gastroenterology & Hepatology, Tokyo Medical University, 6-7-1 Nishishinjuku, Shinjuku-ku, Tokyo, 160-0023, Japan, [2]The Ultrasound Systems Development Department, Toshiba Medical Systems Corporation, 1385, Shimoishigami, Otawara-shi, Tochigi 324-8550, Japan, and [3]Department of Diagnostic Ultrasound, Medical Imaging Center, Hyogo College of Medicine, 1-1 Mukogawa-cho, Nishinomiya, Hyogo 663-8501, Japan

Aim: To determine whether the findings of microflow imaging (MFI), composed of a flash replenishment and a maximum intensity holding sequence, using contrast-enhanced sonography, correlate with the degree of histological differentiation of hepatocellular carcinoma (HCC).

Methods: This study was approved by the institutional review board; patients gave informed consent. The samples comprised of 61 nodules histologically diagnosed as HCC: 20 well-differentiated, 26 moderately-differentiated, and 15 poorly-differentiated HCC. SonoVue was used as the ultrasound (US) contrast agent. The US equipment used was a SSA-770 A with the imaging mode set at MFI. MFI is an imaging method combining flash replenishment imaging and maximum intensity holding. Two independent readers (readers 1 and 2) classified the microflow images into four patterns: (i) normal pattern; (ii) cotton pattern; (iii) vascular pattern; and (iv) dead wood pattern. The results were compared with the degree of histopathological differentiation of the HCC.

Results: In each of the 61 HCC, blood vessels in the tumor were clearly resolved down to their fine branches. With regard to the relationship between imaging patterns and the histological findings, it was found (with high percentages) that the normal and cotton patterns were associated with well-differentiated HCC, that the vascular pattern was associated with moderately-differentiated HCC, and that the dead wood pattern was associated with poorly-differentiated HCC. If HCC with the normal and cotton patterns were assessed as well differentiated and those with the vascular or dead wood pattern were assessed as moderately or poorly differentiated, the sensitivity, specificity, and accuracy of these assessments were found to be 85%, 92.7%, and 90%, respectively, for reader 1, and 85%, 82.9%, and 83.6%, respectively, for reader 2.

Conclusion: The angioarchitecture and hemodynamics of HCC could be evaluated in detail using MFI. The results of this study demonstrate the feasibility of a non-invasive preoperative diagnosis of the histological differentiation of HCC using MFI.

Key words: contrast agent, hepatocellular carcinoma, histological differentiation, microflow imaging, ultrasonography

INTRODUCTION

HEPATOCELLULAR CARCINOMA (HCC) is the most common primary liver cancer, usually occurring as a complication of chronic liver disease and most often arising in a cirrhotic liver.[1–3] Therefore, the accurate surveillance of patients with liver cirrhosis is of great clinical importance because they are at increased risk of HCC.[4] The accurate and early diagnosis of HCC is essential for the treatment of affected patients. Surgical resection, liver transplantation, and percutaneous radiofrequency ablation (RFA) are potentially curative therapies for some patients.[5–8]

The ultrasound (US) findings of a focal liver lesion are often non-specific without contrast. Thus it is necessary to perform dynamic computed tomography (CT) or magnetic resonance imaging (MRI), or both for its characterization.[9–15] In addition to imaging studies, a

Correspondence: Dr Katsutoshi Sugimoto, Department of Gastroenterology and Hepatology, Tokyo Medical University, 6-7-1 Nishishinjuku, Tokyo 160-0023, Japan. Email: sugimoto@comcast.net
Received 21 May 2007; revision 28 December 2007; accepted 3 January 2008.

fine needle biopsy (FNB) is recommended for all nodules with a diameter less than 2 cm, because in these cases it is difficult to distinguish HCC from other conditions using imaging techniques alone.[8]

It is known that more poorly-differentiated HCC are associated with a higher biological grade,[16] and thus determining the degree of differentiation is critical in clinical practice. Vascular invasion is one of the most important determinants of tumor grade and has also been reported to be correlated with the degree of differentiation.[17] It is therefore essential to conduct comprehensive imaging studies, as well as FNB, to diagnose the type and degree of differentiation of tumors. However, concerns have been raised about the risk of seeding during FNB aspiration of HCC in patients who will undergo liver transplantation or surgical resection,[18–20] which has been estimated to be up to 3.4%.[21] Diagnosing the degree of differentiation of HCC without biopsy has therefore been gaining more attention. In addition, while local therapies represented by RFA have recently been used widely, some authors have suggested that patients with poorly-differentiated HCC should be treated by primary surgery, because of the high incidence of local recurrence.[22] Diagnosing the degree of differentiation by imaging studies has therefore been suggested to be essential for determining the therapeutic application.

Recent advances in US technology, including harmonic imaging and the availability of US contrast agents, have improved the usefulness of US in the characterization of focal liver lesions, including HCC.[23–27] In particular, vascular imaging has been used to help determine the tissue type of focal liver lesions. Vascularity and/or morphological changes of the tumor vessels provide diagnostic information. For instance, a spoke wheel structure of the vessels is characteristic of focal nodular hyperplasia. In dynamic contrast US studies, we can observe the tumor vessels in the early arterial phase 10–30 s after an intravenous injection of contrast agent, at which time the tumor parenchyma is not yet opacified with the contrast agent.[28] Except for large-sized blood vessels, most of the vascular structure becomes blurred and obscured in the parenchymal opacification with contrast agents.[28] It is well known that microbubble contrast agents are destroyed by US exposure if the mechanical index (MI) of the transmitting pulse is higher than the microbubble destruction threshold. The flash replenishment sequence (FRS) consists of the destruction of microbubbles in the scan volume under exposure to a high MI US and visualization of reperfusion filled with fresh microbubbles under low MI harmonic imaging. This has been used for vascular imaging and quantitative analysis of myocardial perfusion[29] and hepatic parenchymal blood flow.[30] Microflow imaging (MFI; Toshiba Medical Systems, Otawara, Japan) was developed because the combination of FRS and the maximum intensity holding sequence was expected to make it possible to visualize vascular structure with high special resolution and vascular continuity. To our knowledge, this is the first study correlating the findings of MFI using SonoVue (Bracco, Milan, Italy), a second-generation US contrast agent, with the degree of cellular differentiation.

The aim of this study was to determine whether the MFI findings correlate with the degree of cellular differentiation.

METHODS

Study population

THE STUDY INCLUDED 61 patients with HCC ranging from 8 to 50 mm (mean ± SD, 21.5 ± 10.9 mm) that had been clearly visualized on conventional sonograms for the first time during the 18 months from July 2005 to December 2006. The patients included were 34 men and 27 women with an age range of 41–83 years (mean age, 70.7 ± 7.9 years). For patients with more than one focal lesion with a similar appearance at baseline gray-scale US, we selected the largest and most conspicuous lesion for this study. This study had the approval of the institutional ethics review board of Tokyo Medical University, Tokyo, Japan; all patients gave informed consent. Specimens from hepatic masses were obtained with a 20-gauge US-guided FNB. The degree of cellular differentiation (defined as well-, moderately-, or poorly-differentiated HCC) was determined according to the International Working Party classification.[31]

Sonologists

Three sonologists from our institution, who had 8 (KS), 20 (FM), and 15 (M.Y) years of experience in liver US imaging were involved in this study. Each sonologist had at least 5 years of experience in microbubble contrast, material-enhanced US of the liver, was aware of the patients' clinical histories, and was blinded to the biopsy results.

Sequence for MFI

A schematic illustration of MFI is shown in Figure 1. The FRS was performed manually by the operator. The maximum-hold processing started just after the burst

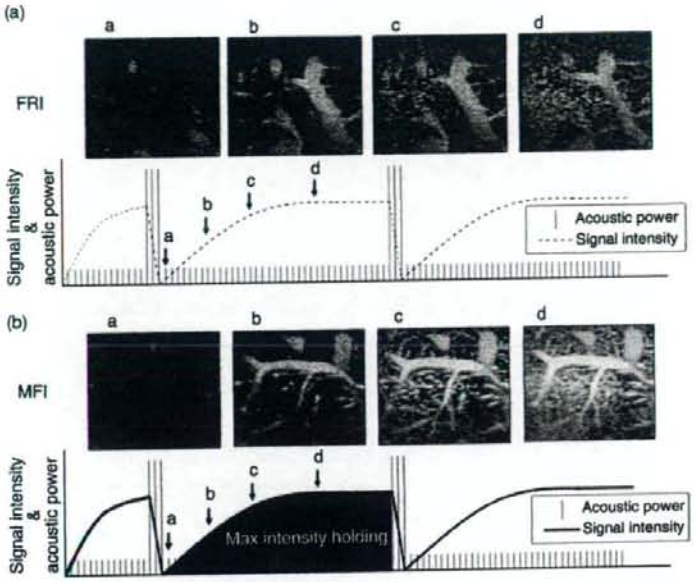

Figure 1 Scan sequences of (a) flash replenishment imaging (FRI) and (b) microflow imaging (MFI). Acquisition signals during replenishment after high mechanical index burst scanning are depicted with the maximum intensity holding technique in the MFI sequence. Each microbubble is recognized on the FRI images. However, continuous visualization of small blood vessels markedly improves on MFI images. (a) Acoustic power (|), Signal intensity (----); (b) Acoustic power (|), Signal intensity (—).

scan. The burst scan consisted of high MI (1.3–1.6) scanning of five frames. Low MI (0.07–0.09) scanning started again just after the high MI burst scanning to visualize fresh microbubble contrast agents flowing into the scanning volume.

The maximum intensity holding sequence was started simultaneously with flash replenishment low MI imaging, which maintained maximum brightness on each pixel and was displayed as a persistent vision. When the next burst scan was performed, max-hold processing was reset and this process was repeated several times to see the liver parenchyma and tumor tissue perfusion. The accumulation time for each MFI sequence was 10–15 s, depending on the perfusion of the target tissue.

Imaging techniques

SonoVue, the contrast agent used in this study, consists of sulfur hexafluoride microbubbles surrounded by phospholipids. The average diameter of a microbubble is 2.5 μm. SonoVue was injected as a 1.5 mL bolus into an antecubital vein using a 21-gauge peripheral intravenous cannula, followed by an injection of 10 mL saline solution at a rate of 1.0 mL/s. The US equipment used was a SSA-770 A (Aplio, Toshiba Medical Systems, Japan) with a 3.75 MHz convex transducer (PSK-375BT). The imaging mode was wideband harmonic imaging (commercially called pulse subtraction) with transmission and reception frequencies of 3.75 and 7.5 MHz, respectively. When a suspected lesion was identified, a dynamic contrast-enhanced ultrasonography (CEUS) was performed with the focus depth beyond the region of interest using the following settings: frame rate, 15 fps, and dynamic range, 35 dB. A low MI (0.07–0.09) was selected to avoid the disruption of microbubbles.

The region of interest was observed continuously for approximately 3 min from the time of injection. The arterial phase was timed for 45 s after the completion of the flash, after which we defined an extended portal venous phase, and this phase encompassed the commonly described interval from 45 to 70 s after injection, as well as the remainder of the observation period. Because the microbubbles of the contrast agent were purely intravascular, there was no interstitial or equilibrium phase. Enhancement in the extended portal venous phase showed progressive decay during approximately 3 min until the baseline appearance was observed again.[32]

We performed MFI once at the arterial phase and twice at the portal venous phase. Images and clips were stored on the hard disk for offline analysis. Among the three microflow (MF) images thus obtained, the MF image in which the vascular architecture was most clearly visualized was selected (KS) and kept for later

analyses. Data obtained in dynamic studies other than MFI were excluded from the analyses.

Retrospective analysis

Digital cine clips stored on a PC were reviewed retrospectively on screen by two independent readers (RM and YI). Both were sonologists with 5 (RM) and 10 (YI) years of experience in using microbubble contrast agents. They were not involved in the US scanning. These readers were blinded to the identification, clinical histories, biopsy results, and other imaging findings of the patients. Cine clips were presented in random order, and any identifying information was masked. Prior to the reading, the readers were shown eight similar examples of MFI to establish a standardized approach to the interpretation of the information provided in the imaging sequences. The two readers were requested to classify each image as one of the following four patterns: normal, cotton, vascular, and dead wood patterns. In the normal pattern, the border between tumoral and non-tumoral regions was slightly indistinct, and the vascular architecture in the tumoral region was similar to that in the adjacent non-tumoral region (Fig. 2c). In the cotton pattern, the border between the tumoral and non-tumoral regions was distinct, but tumoral blood vessels were not clearly visualized and the tumor appeared pale as a whole, as if it was stained (Fig. 3c). In the vascular pattern, tortuous and meandering tumoral blood vessels were visualized clearly, and the tumor was imaged pronouncedly as a whole (Fig. 4c). In the dead wood pattern, tumoral blood vessels were visualized clearly, but they gradually tapered off and were interrupted suddenly (Fig. 5c). As a result, the distribution of the blood vessels was spatially heterogeneous in the tumor.

Statistical analyses

Statistical analyses were performed with a computer software package (StatMate III for Windows; Atoms, Tokyo, Japan). Baseline characteristics of the patients and HCC are expressed as mean ± SD. The relationship between the tumor size and pathological grading was analyzed with Fisher's exact test. A value of $P < 0.05$ was considered statistically significant. Sensitivity was defined as TN/(TN + FN), specificity as TN/(TP + FP), and overall accuracy as (TP + TN)/(TP + TN + FP + FN), where TP is the number of true positive diagnoses, FN is the number of false negative diagnoses, TN is the number of true negative diagnoses, and FP is the number of false positive diagnoses.

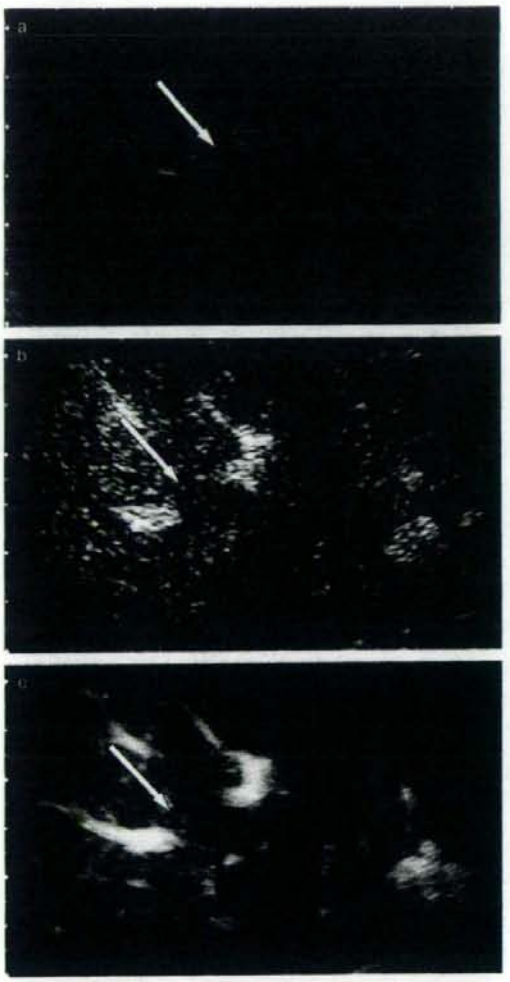

Figure 2 A 77-year-old woman with a 10-mm-diameter, well-differentiated hepatocellular carcinoma (HCC) in the right lobe of her liver. (a) Baseline ultrasound image show a focal hypoechoic HCC (arrow) in the right hepatic lobe. (b) Conventional harmonic image obtained during the portal venous phase—that is, 46 s after injection of the microbubble contrast agent—shows HCC (arrow) with an iso or slightly hypoechoic appearance relative to the adjacent liver. (c) Microflow image obtained during the portal venous phase—that is, 50 s after injection of the microbubble contrast agent—shows the blood vessel architecture more distinctly than the conventional harmonic image. Border between the tumoral and normal regions is not distinct. Blood vessel architecture in the tumoral region is almost identical with that in the adjacent normal hepatic parenchyma. Properties are characteristic of the normal pattern.

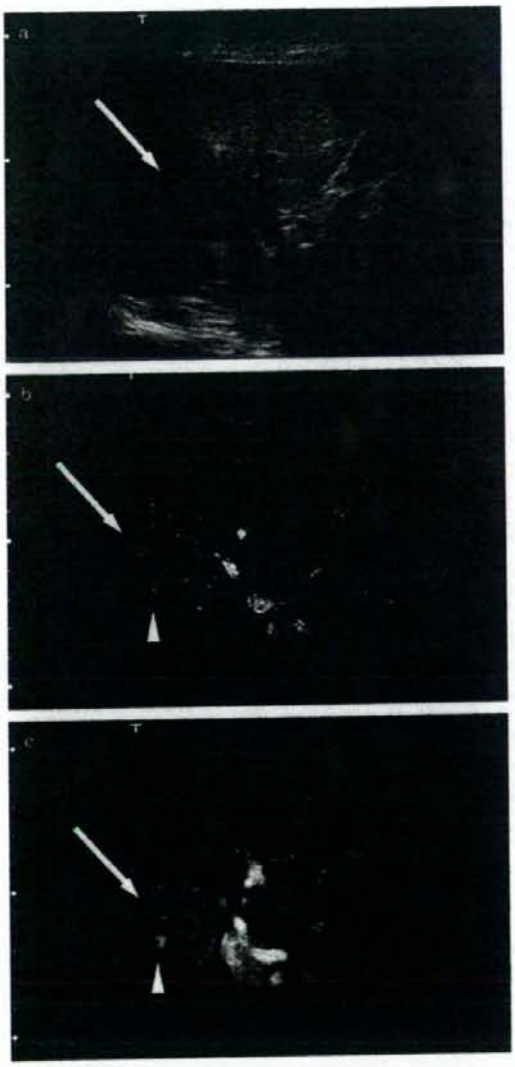

Figure 3 A 75-year-old man with a 28-mm-diameter, well-differentiated hepatocellular carcinoma (HCC) in the right lobe of his liver. (a) Baseline ultrasound image shows a HCC (arrow) with mosaic pattern appearance in the right hepatic lobe. (b) Conventional harmonic image obtained during the arterial phase—that is, 25 s after injection of the microbubble contrast agent—shows HCC (arrow) with a slightly hyperechoic appearance relative to the adjacent liver. Nodule-in-nodule appearance (arrow head) is demonstrated as a hypervascular spot in a slightly hypervascular nodule. (c) Microflow image obtained during the arterial phase—that is, 30 s after injection of the microbubble contrast agent—shows the blood vessel architecture more distinctly than the conventional harmonic image. Border between the tumoral and non-tumoral regions is distinct, but tumoral blood vessels are not clearly visible. Contrast-enhanced image of the tumoral region looks as if it was stained. Properties are characteristic of the cotton pattern. Nodule-in-nodule appearance (arrow head) is also more visible than in the conventional harmonic image.

RESULTS

Technical performance

A TOTAL OF 61 examinations were analyzed. All examinations were technically satisfactory for MFI.

Histological findings

The final diagnoses of the HCC were as follows: well-differentiated HCC in 20 cases (32.8%), ranging in diameter from 8 to 22 mm (mean ± SD, 15.3 ± 4.6 mm), moderately-differentiated HCC in 26 cases (42.6%), ranging in diameter from 10 to 40 mm (mean ± SD, 20.7 ± 8.5 mm), and poorly-differentiated HCC in 15 cases (24.6%), ranging in diameter from 15 to 50 mm (mean ± SD, 31.3 ± 13.8 mm). The results of tumor size and histopathology are shown in Table 1. The tumor size was significantly larger in poorly-differentiated HCC than in the other HCC ($P < 0.01$ for well-differentiated HCC, $P < 0.05$ for moderately differentiated HCC). In total, 100% (20/20) of well-differentiated HCC were smaller than 30 mm, 88.5% (23/26) of moderately-differentiated HCC were smaller than 30 mm, and 46.7% (7/15) of poorly-differentiated HCC were larger than 30 mm.

Blinded reading

The two independent readers classified the MF images into the four patterns, that is, normal, cotton, vascular, and dead wood. Their results were compared with the degree of histopathological differentiation of HCC. With both readers 1 (Table 2) and 2 (Table 3), there were trends for the normal and cotton patterns to be associated with well-differentiated HCC, the vascular pattern to be associated with moderately-differentiated HCC, and the dead wood pattern to be associated with poorly-differentiated HCC. In addition, neither reader found moderately- or poorly-differentiated HCC exhibiting the normal pattern or well-differentiated HCC exhibiting the dead wood pattern. If HCC with normal

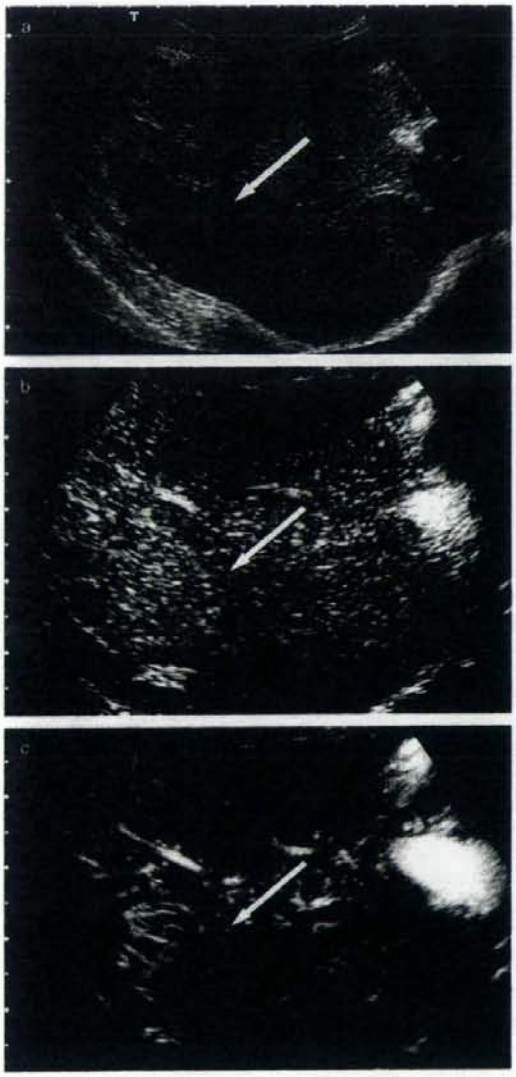

Figure 4 A 78-year-old man with a 30-mm-diameter, moderately-differentiated hepatocellular carcinoma (HCC) in the right lobe of his liver. (a) Baseline ultrasound image shows a focal hypoechoic HCC (arrow) in the right hepatic lobe. (b) Conventional harmonic image obtained during the portal venous phase—that is, 50 s after injection of the microbubble contrast agent—shows HCC (arrow) with homogeneous enhancement relative to the adjacent liver. (c) Microflow image obtained during the portal venous phase—that is, 55 s after injection of the microbubble contrast agent—shows the blood vessel architecture more distinctly than the conventional harmonic image. Border between the tumoral (arrow) and non-tumoral regions was distinct. Proliferation of tortuous and meandering blood vessels is clearly visible. Properties are characteristic of the vascular pattern.

and cotton patterns were assessed to be well differentiated and those with vascular or dead wood patterns were assessed to be moderately or poorly differentiated, the sensitivity, specificity, and accuracy of such assessments were found to be 85%, 92.7% and 90%, respectively, for reader 1, and 85%, 82.9%, and 83.6%, respectively, for reader 2 (Table 4).

DISCUSSION

THE DEVELOPMENT OF HCC is characterized by angiogenesis and the detection of new arterial vasculature in a focal liver lesion in a cirrhotic liver aids in the identification of HCC. HCC is a hypervascular tumor best diagnosed by spiral dynamic CT and dynamic MRI, because both techniques can evaluate the vascularity of the tumor using contrast enhancement.[9–15] Under dynamic CT or MRI, HCC typically presents a hypervascular pattern in the arterial phase and wash out in the late phase. However, the equipment required for such evaluations may not be available in small peripheral hospitals, and these procedures are usually more expensive than US. In addition, CT has the potential risk of radiation exposure.

Microbubble-based US contrast agents increase the intensity of the blood flow signal, improving the detection of flow in the hepatic artery and small vessels, and are as effective as CT contrast agents in assessing lesion perfusion.[23] Contrast-specific modes, such as advanced dynamic flow (ADF, Toshiba Medical Systems, Japan), associated with the contrast agent Levovist (Schering AG, Berlin, Germany), allow the evaluation of microvascularization of focal liver lesions, improving their characterization.[33] However, because Levovist's microbubbles are too sensitive to the US pulse, intermittent scanning (i.e. non-real-time imaging method) has to be used.[23] The new contrast agents, such as SonoVue, are more stable and resistant to US exposure and radiate sufficient harmonic signals by low MI transmission power, which allows continuous real-time imaging.[34] Also, from a clinical point of view, the real-time examination with SonoVue can acquire detailed information and time efficiency for the examination

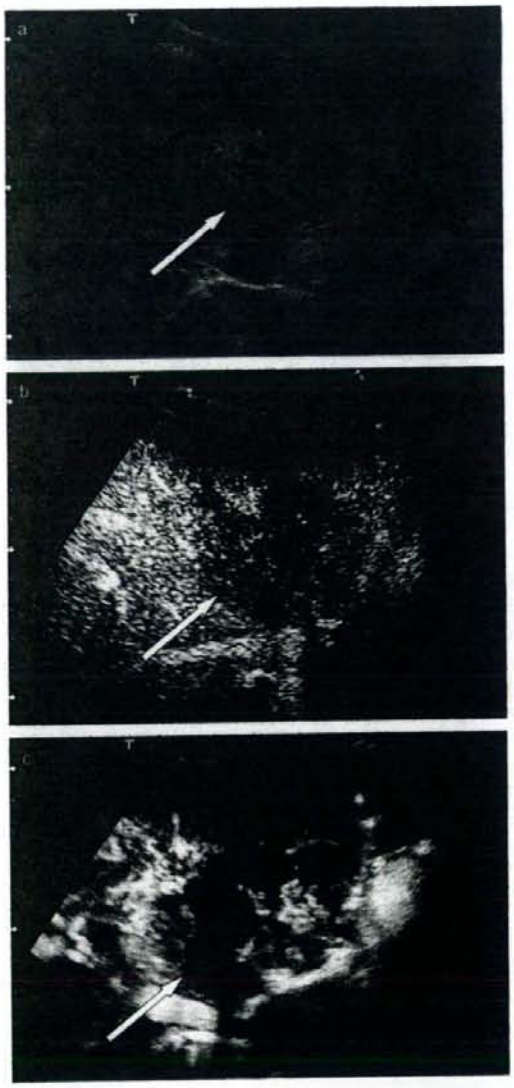

Figure 5 A 69-year-old woman with a 50-mm-diameter, poorly-differentiated hepatocellular carcinoma (HCC) in the left lobe of her liver. (a) Baseline ultrasound image shows a HCC (arrow) with mosaic pattern appearance in the left hepatic lobe. (b) Conventional harmonic image obtained during the portal venous phase—that is, 48 s after injection of the microbubble contrast agent—shows HCC (arrow) with heterogeneous enhancement. An avascular area, which is believed to be a necrotic region, is also noted in the tumor. (c) Microflow image obtained during the portal venous phase—that is, 53 s after injection of the microbubble contrast agent—shows tumoral blood vessels clearly. However, they are sparser than in moderately-differentiated HCC. Tapering and interruption of the vessels may be noted. Properties are characteristic of the dead wood pattern.

itself. It is suggested to be superior to Levovist in the evaluation of the hemodynamic status of focal liver lesions.

Several authors have reported on the behavior of the microbubbles in HCC.[23,24,26,27,34] Solbiati *et al.*[34] described a diffuse enhancement during the arterial phase that decreases during the portal venous and late phases, presenting a hypoechoic appearance in 54 of 61 HCC (88.5%), while in the remaining seven, they found a non-homogeneous enhancement related to necrotic changes. Nicolau *et al.*[35] reported that almost all HCC (96.2%) showed intratumoral enhancement in the arterial phase with a wash out in the late phase in 74 of 104 HCC (71.2%). Four HCC in their study without arterial enhancement in the CEUS were found to be well-differentiated HCC. They also found significant differences between the degree of cellular differentiation in the enhancement pattern of the HCC in the portal and late phases. Fan *et al.* also reported that moderately- to poorly-differentiated HCC had significantly shorter wash-out times compared to well-differentiated HCC, suggesting that CEUS is useful for determining the degree of differentiation of HCC[36]

In these studies, HCC was diagnosed on the basis of the degree of contrast enhancement of the tumor in the arterial phase and the degree of wash out in the portal and late phases. In the present study, we used MFI, a new imaging method developed by combining FRS and max intensity holding, and observed the fine architecture of blood vessels in the tumor and changes in their distribution, and thereby diagnosed HCC.

MF images could be classified into the following four patterns: normal, cotton, vascular, and dead wood patterns. Two readers classified each MF image into one of these four patterns, and the degree of histological differentiation of each lesion was compared with the pattern of its MF image. There were trends that the normal and cotton patterns were found in well-differentiated HCC, he vascular pattern was found in moderately-differentiated HCC, and the dead wood pattern was found in poorly-differentiated HCC. This result sug-

Table 1 Tumor size and histopathology of 61 lesions

Histological differentiation	Tumor size (mm)				
	<20	20–30	31–40	41–50	Total
Well-differentiated HCC	13	7	0	0	20
Moderately-differentiated HCC	13	10	3	0	26
Poorly-differentiated HCC	4	4	3	4	15
Total	30	21	6	4	61

Tumor size was significantly greater in poorly-differentiated hepatocellular carcinoma (HCC) than in other HCC. ($P < 0.01$ for well-differentiated HCC, $P < 0.05$ for moderately-differentiated HCC).

gested the possibility that the degree of histopathological differentiation of HCC could be assessed with considerable accuracy using MFI.

According to a histological examination of HCC by Ueda *et al.*,[37] the portal region in nodules (including the normal portal vein and the hepatic artery) decreased in size, while increasing the malignancy of HCC, and became unobservable in moderately- and poorly-differentiated HCC. A few unpaired arteries, which took courses independent of the bile duct, that is, abnormal- or newly-growing arteries, were observed in atypical adenomatous hyperplasia. The unpaired arteries gradually increased in number with increasing malignancy of the tumor, and proliferated markedly in moderately-differentiated HCC.

It is conceivable therefore that even though the portal region partially decreases in size in well-differentiated HCC, this stage still has a recognizable portal region and only a few unpaired arteries. This stage seems to correspond to the normal and cotton patterns. According to Kojiro *et al.*,[38] small HCC less than approximately 2 cm in diameter may be grossly classified into two major types: a vaguely nodular type and a distinctly nodular type. They are markedly different from each other not only morphologically, but also biologically. In the present study, needle biopsies were used to obtain specimens for the histological examination. Differentiating tumors of the vaguely nodular type from those of the distinctly nodular type was consequently difficult. It seems to be possible, however, that the normal pattern

Table 2 MFI patterns of HCC according to histological differentiation (reader 1)

Histological differentiation	MFI patterns (reader 1)				Total
	Normal	Cotton	Vascular	Dead wood	
Well-differentiated HCC	8	9	3	0	20
Moderately-differentiated HCC	0	3	21	2	26
Poorly-differentiated HCC	0	0	3	12	15
Total	8	12	27	14	61

All data are actual values. HCC, hepatocellular carcinoma; MFI, microflow imaging.

Table 3 MFI patterns of HCC according to histological differentiation (reader 2)

Histological differentiation	MFI patterns (reader 2)				Total
	Normal	Cotton	Vascular	Dead wood	
Well-differentiated HCC	10	7	3	0	20
Moderately-differentiated HCC	0	6	18	2	26
Poorly-differentiated HCC	0	1	8	6	15
Total	10	14	29	8	61

All data are actual values. HCC, hepatocellular carcinoma; MFI, microflow imaging.

Table 4 Diagnostic performance of MFI at retrospective analysis

Performance parameter	MFI	
	Reader 1	Reader 2
Sensitivity	85.0 (17/20)	85.0 (17/20)
Specificity	92.7 (38/41)	82.9 (34/41)
Accuracy	90.2 (55/61)	83.6 (51/61)

Hepatocellular carcinoma with normal and cotton patterns were found to be well-differentiated and those with vascular or dead wood patterns were assessed to be moderately or poorly differentiated.
All data are percentages. Unless stated, numbers in parentheses are the numbers of lesions used to calculate the percentage. MFI, microflow imaging.

corresponded to the vaguely nodular type (early-stage HCC),[39] whereas the cotton pattern corresponded to the distinctly nodular type. The vascular pattern in the classification of MF images seems to reflect the next stage in malignancy, in which unpaired arteries have proliferated and the portal region has disappeared. With further progression of malignancy, feeding arteries are infiltrated by tumor cells located nearby or by cells in embolic tumors, and efferent vessels are blocked by tumoral emboli. As a result, circulatory disorders occur and blood flow in the tumor becomes spatially heterogeneous. The dead wood pattern seems to represent this stage. The histopathological changes described in this paragraph are considered to provide a background for the results of the present study.

The principal limitation of this study was that specimens for histopathological diagnosis of the degree of differentiation of HCC were obtained by FNB. The specimen obtained by FNB allows us to evaluate only a small part of the HCC lesion, which had been produced through a process called multistep hepatocarcinogenesis, that is, the successive development of the well-differentiated HCC from the dysplastic nodule through the dysplastic nodule with malignant foci, and consequently had histopathological heterogeneity inside. However, surgical verification is obtained infrequently, especially in patients with HCC, because small HCC lesions are often treated with transcatheter arterial chemoembolization or percutaneous ablation, especially in cirrhotic patients whose functional reserve is severely impaired.

A second limitation was that MFI has been clinically available to reconstruct the fine structure of the tumor vessels using the maximum intensity projection method. However, careful image acquisition is required when constructing MFI, that is, to avoid the blur due to the motion of both probe position and patient breathing. However, automatic motion correction devices are being developed to overcome this problem. Consequently, the problem of motion artifacts is expected to be resolved in the near future.

As for the safety of the contrast agent, no adverse reactions were observed in any patients in this study. Unlike the contrast agents used for CT imaging, SonoVue is non-iodine based and the injected volume is at most 5 mL. Therefore, possible adverse reactions, such as an allergic reaction to iodine or renal or cardiac overload, are less likely to occur.

In conclusion, the angioarchitecture and hemodynamics of HCC could be evaluated in detail using MFI. The results of this study show the feasibility of non-invasive preoperative diagnosis of histological differentiation of HCC using CEUS, with a high degree of accuracy and objectivity.

REFERENCES

1 Di Bisceglie AM. Hepatitis C and hepatocellular carcinoma. *Hepatology* 1997; **26**: 34S–38S.
2 El-Serag HB, Mason AC. Rising incidence of hepatocellular carcinoma in the United States. *N Engl J Med* 1999; **340**: 745–50.
3 Colombo M. Hepatocellular carcinoma. *J Hepatol* 1992; **15**: 225–36.
4 Collier J, Sherman M. Screening for hepatocellular carcinoma. *Hepatology* 1998; **27**: 273–8.
5 Trinchet JC, Beaugrand M. Treatment of hepatocellular carcinoma in patients with cirrhosis. *J Hepatol* 1997; **27**: 756–65.
6 Bruix J. Treatment of hepatocellular carcinoma. *Hepatology* 1997; **25**: 259–62.
7 Mor E, Kaspa RT, Sheiner P, Schwartz M. Treatment of hepatocellular carcinoma associated with cirrhosis in the era of liver transplantation. *Ann Intern Med* 1998; **129**: 643–53.
8 Bruix J, Sherman M, Llovet JM *et al.* Clinical management of hepatocellular carcinoma: conclusions of the Barcelona 2000 EASL Conference. *J Hepatol* 2001; **35**: 421–30.
9 Takayasu K, Moriyama N, Muramatsu Y *et al.* The diagnosis of small hepatocellular carcinomas: efficacy of various imaging procedures in 100 paients. *AJR* 1990; **155**: 49–54.
10 Szklaruk J, Silverman PM, Charnsangavej C. Imaging in the diagnosis, staging, treatment, and surveillance of hepatocellular carcinoma. *AJR* 2003; **180**: 441–54.
11 Lee HM, Lu DS, Krasny RM, Busuttil R, Kadell B, Lucas J. Hepatic lesion characterization in cirrhosis: significance of arterial hypervascularity on dual-phase herical CT. *AJR* 1997; **169**: 125–30.

12 Teefey A, Hildeboldt CC, Dehdashti F *et al.* Detection of primary hepatic malignancy in liver transplant candidates: prospective comparison of CT, MR imaging, US, and PET. *Radiology* 2003; **226**: 533–42.
13 Baron RL, Oliver JH III, Dodd GD III, Nalesnik M, Holbert BL, Carr B. Hepatocellular carcinoma: evaluation with biphasic, contrast-enhanced, helival CT. *Radiology* 1996; **199**: 505–11.
14 Miller WJ, Baron RL, Dodd GD 3rd, Federle MP. Malignancies in patients with cirrhosis: CT sensitivity and specificity in 200 consecutive transplant patients. *Radiology* 1994; **193**: 645–50.
15 Brancatelli G, Baron RL, Pererson MS, Marsh W. Helical CT screening for hepatocellular carcinoma in patients with cirrhosis: frequency and causes of false-positive interpretation. *AJR* 2003; **180**: 1007–14.
16 Kojiro M. Histopathology of liver cancers. *Best Pract Res Clin Gastroenterol* 2005; **19**: 39–62.
17 Sun B, Zhang S, Zhang D *et al.* Vasculogenic mimicry is associated with high tumor grade, invasion and metastasis, and short survival in patients with hepatocellular carcinoma. *Oncol Rep* 2006; **16**: 693–8.
18 Kanematsu M, Hoshi H, Takao H, Sugiyama Y. Abdominal wall tumor seeding at sonographically guided needle-core aspiration biopsy of hepatocellular carcinoma. *AJR* 1997; **169**: 1198–9.
19 Takamori R, Wong LL, Dang C, Wong L. Needletract implantation from hepatocellular cancer: is needle biopsy of the liver always necessary? *Liver Transpl* 2000; **6**: 67–72.
20 Torzilli G, Minagawa M, Takayama T *et al.* Accurate preoperative evaluation of liver mass lesions without fine-needle biopsy. *Hepatology* 1999; **30**: 889–93.
21 Kim SH, Lim HK, Lee WJ, Cho JM, Jang HJ. Needle-tract implantation in hepatocellular carcinoma: frequency and CT findings after biopsy with a 19.5-gauge automated biopsy gun. *Abdom Imaging* 2000; **25**: 246–50.
22 Yu HC, Cheng JS, Lai KH *et al.* Factors for early tumor recurrence of single small hepatocellular carcinoma after percutaneous radiofrequency ablation therapy. *World J Gastroenterol* 2005; **11**: 1439–44.
23 Numata K, Tanaka K, Kiba T *et al.* Contrast-enhanced, wide-band harmonic gray scale imaging of hepatocellular carcinoma. *J Ultrasound Med* 2001; **20**: 89–98.
24 Wilson SR, Burns PN, Murdali D *et al.* Harmonic hepatic US with microbubbles contrast agents: initial experience showing improved characterization of hemangioma, hepatocellular carcinoma and metastasis. *Radiology* 2000; **215**: 147–51.
25 Choi BI, Kim TK, Han JK, Kim AY, Chang KS, Park JP. Vascularity of hepatocellular carcinoma: assessment with contrast-enhanced second harmonic versus conventional power Doppler US. *Radiology* 2000; **214**: 381–6.
26 Kim TK, Choi BI, Han JK, Hong HS, Park SH, Moon SG. Hepatic tumor: contrast agent-enhancement patterns with pulse-inversion harmonic US. *Radiology* 2001; **216**: 411–17.
27 Tanaka S, Ioka T, Oshikawa O, Hamada Y, Yoshioka F. Dynamic sonography of hepatic tumors. *AJR* 2001; **177**: 799–805.
28 Sirlin CB, Girard MS, Baker KG, Steinbach GC, Deiranieh LH, Mattrey RF. Effect of acquisition rate on liver and portal vein enhancement with microbubble contrast. *Ultrasound Med Biol* 1999; **25**: 331–8.
29 Wei K, Jayaweera AR, Firoozan S *et al.* Quantification of myocardial blood flow with ultrasound-induced destruction of microbubbles administrated as a contrast venous infusion. *Circulation* 1998; **97**: 473–83.
30 Metoki R, Moriyasu F, Kamiyama N *et al.* Quantification of hepatic parenchymal blood flow by contrast ultrasonography with flash-replenishment imaging. *Ultrasound Med Biol* 2006; **32**: 1459–66.
31 International Working Party. Terminology of nodular hepatocellular lesions. *Hepatology* 1995; **22**: 983–93.
32 Burns PN, Wilson SR. Focal liver masses: enhancement patterns on concordance of US scans with CT scans and MR images. *Radiology* 2007; **242**: 162–74.
33 Hotta N, Tagava T, Maeno T *et al.* Advanced dynamic flow imaging with contrast-enhanced ultrasonography for the evaluation of tumor vascularity in liver tumors. *Clin Imaging* 2005; **29**: 34–41.
34 Solbiati L, Tonillini M, Cova L, Goldberg N. The role of contrast-enhanced ultrasound in the detection of focal liver lesions. *Eur Radiol* 2001; **11**: E15–26.
35 Nicolau C, Catala V, Vilana R *et al.* Evaluation of hepatocellular carcinoma using SonoVue, a second generation ultrasound contrast agent: correlation with cellular differentiation. *Eur Radiol* 2004; **14**: 1092–9.
36 Zhi-Hui Fan, Min-HuaChen Ying Dai et al. Evaluation of primary malignancies of liver using contrast-enhanced sonography: correlation with pathology. *AJR* 2006; **186**: 1512–19.
37 Ueda K, Terada T, Nakanuma Y *et al.* Vascular supply in adenomatous hyperplasia of the liver and hepatocellular carcinoma: a morphologic study. *Hum Pathol* 1992; **23**: 619–26.
38 Kojiro M, Nakashima O. Histopathologic evaluation of hepatocellular carcinoma with a special reference to small early stage tumor. *Semin Liver Dis* 1999; **19**: 287–96.
39 Liver Cancer Study Group of Japan. *General Rules for the Clinical and Pathological Study of Primary Liver Cancer*, 2nd edn. Tokyo: Kanehara, 2003.

特集
最新の肝胆膵の3Dイメージ
胆と膵 Vol. 29 臨時増刊特大号 p. 1173～1180, 2008

肝臓の造影超音波
－3Dイメージから4Dイメージ－*

山田 昌彦[1]・森安 史典[1]

要約：3次元超音波（3D-US）は2次元画像から3次元画像を構築し，いわばレトロスペクティブに画像を見て診断する検査であったが，現在ではリアルタイムに3D画像を表示できるまでに装置が進歩した。リアルタイム3D超音波（4D-US）は，産科領域や循環器科領域では普及しているが，腹部領域では4D-USには高い関心が寄せられているものの，その適応や有用性に関しては未だ研究段階の部分も多く，開発の余地を残している。ソナゾイドの開発およびこれに対応した低音圧を用いた造影超音波モードが開発され，レボビストに比較して高いフレームレートで観察でき，実時間性が大きく向上した。また，レボビストのようにマイクロバブルを壊すことなく超音波検査を行えるため，造影超音波のためのデータが大幅に増加し，空間分解能が向上した。今回われわれは，ソナゾイドを用い，肝腫瘍を対象として4D-USを行った。更に肝癌のRFA治療の効果判定も試みた。4D-USは，B-modeではリアルタイムにMPR表示をできるため，腫瘍や肝の立体構造を即座に理解することに有用であり，さらに，造影4D-USは造影態度を立体的に把握することに有用であった。肝腫瘍の診断においては，血管相の観察が有用であり，RFAの治療後の効果判定には，血管相とともに実質相が有用であった。また，RFAの穿刺においては，4D-USは，3次元的なズレを把握することを容易とした。

Key words：リアルタイム3次元超音波，造影超音波，肝腫瘍，ラジオ波焼灼術

Ⅰ．背 景

a．超音波断層法の進化と造影超音波の開発

超音波断層法は1970年代に臨床応用されたが，長く非造影のBモード断層の時代があり，その後超音波のドプラ効果を利用したドプラモードがそれに加わった。ドプラ信号をBモードに重ねるカラードプラ法は，ドプラ法の2次元断層法として血流の可視化に臨床応用された。対象は，腫瘍の血管を可視化することによる良悪性の鑑別診断や，血管病変の診断である。しかし，腹部の超音波で用いられる周波数，3～4 MHzの変移周波数を画像表示する場合では，表示される血流速度は5 mm/秒以上である。したがって細動脈～毛細血管に至る微小循環の血流表示はできなかった。主に水からなる生体において，生体と最も音響インピーダンスに差があるのは気体である。そこで，血流からの信号を増感するために，毛細血管を容易に通過する微小気泡からなる超音波造影剤が開発された。さらに，非線形信号を映像化するハーモニック技術が開発され，大血管から毛細血管まで，その中を流れる血流を映像化することができるようになった[1]。

また，微小気泡の造影剤のレボビストおよびソナゾイドは，血管から間質へは出ないものの，血管内腔にあるマクロファージによって貪食を受ける。貪食されて細胞内にある微小気泡を映像化することによって，

* Contrast-enhanced Real-time Three-dimensional Ultrasonography of Liver Tumors

1）東京医科大学 消化器内科（〒160-0023 新宿区西新宿6-7-1）

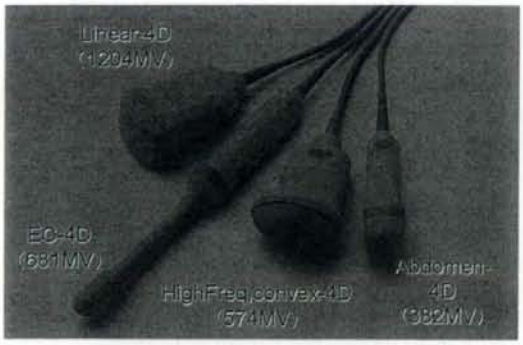

図 1 東芝メカニカル 4D プローブ
今回は右の 382MV を用いた。

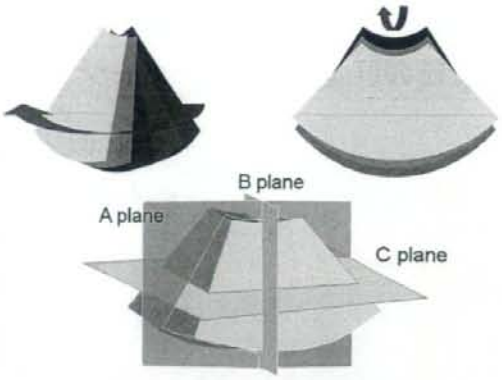

図 2 3D および 4D-US の撮像方法
ボリュームは図の上段のようにスウィープして得られた画像をレンダリングしたもの。MPR ではこれを図のように A 面，B 面，C 面として観察した。

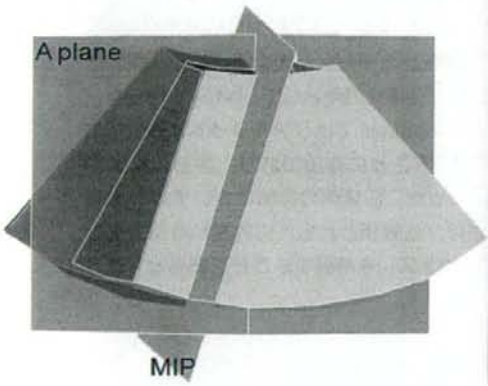

a|b

図 3 穿刺時に用いた VolPure モード
a：B 面を穿刺ラインに沿って傾けたシェーマ。
b：寒天と半熟の鶏卵から作ったファントム。左は A 面で，右は A 面に直交し，穿刺ラインを含む面の MIP 表示。

マクロファージの可視化すなわち細胞標的イメージングが可能となった。内皮側にあるマクロファージの代表的なものは肝臓の Kupffer 細胞である。したがってこれらの，貪食を受ける微小気泡の造影剤は，従来の血管内血流の増感剤である blood pool agent と，細胞標的造影剤である Kupffer cell agent としての 2 つの造影効果を持つことになる。それ故，これらの造影剤は肝臓の超音波検査において多くの情報を与えてくれることになった[2]。

ソナゾイドは 1980 年代からノルウエイの Nycomed 社が開発を始め，欧米で肝臓の腫瘍性疾患の診断のための臨床治験も行われたが，申請までには至らなかった。日本では，ソナゾイドは第一製薬（現第一三共製薬）が開発を進め，第 2 世代造影剤としては本邦では初めて，2007 年 1 月 10 日に世界に先駆けて日本で承認・市販された。承認時のソナゾイドの適応症は，肝腫瘍診断であり，他の臓器の診断は保険適応外である。しかしソナゾイドは，blood pool agent として，他の臓器の腫瘍診断，たとえば膵癌，乳癌，腎癌などの診断にも高い診断能を有する。

b. 3D および 4D 超音波の開発

超音波診断装置の画像処理能力の向上と画像処理技術の進歩により，超音波技術も飛躍的な進歩を遂げた。3 次元超音波検査（3D-US）は連続した 2 次元の断層画像から 3D 画像を構築し，いわばレトロスペクティブに画像を見て診断する検査であった。初期に

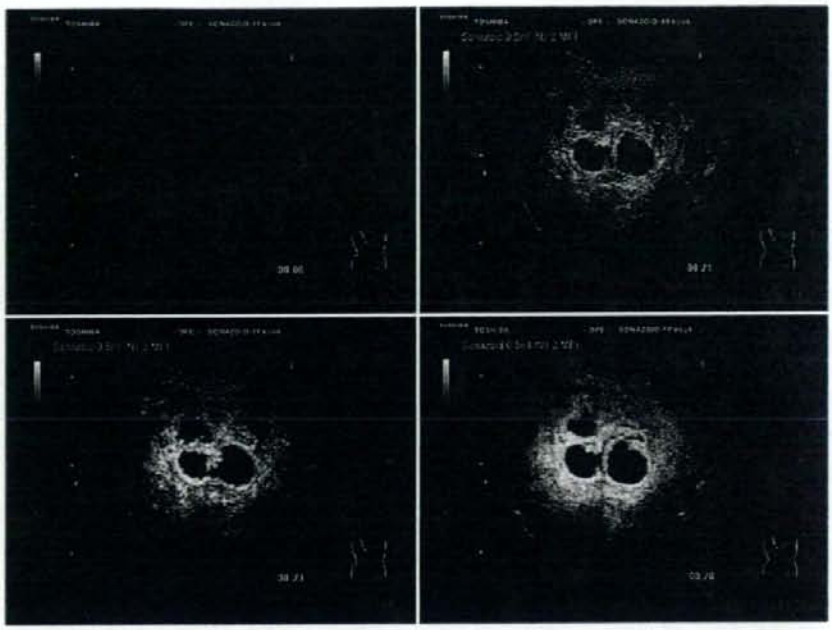

図 4　肝膿瘍のソナゾイド造影 2D-US
a：Bモード像。
b：造影 US の 21 秒後。
c：造影 US の 23 秒後。
d：造影 US の 28 秒後。
膿瘍腔の周囲および境界に高血流な部分が観察された。

は，プローブを手動で Sweep して，連続的に断面を保存し，プローブの移動距離と振り角を入力することにより 3D 画像をレンダリングしていた。その後，位置情報を画像に付加できる磁気センサー付きのプローブが開発され，プローブを Sweep することにより得られた連続断面のそれぞれに自動的に位置情報が付加され，3D 画像を自動的にレンダリングすることができるようになった。さらに，近年はプローブの内部で自動的に Sweep を行うメカニカル 4D プローブが開発され（図 1），腹部用の比較的細径のプローブもでき，自動的に正確な位置情報が付加された連続断面から瞬時に 3D 画像をレンダリングし，腹部領域でも容易に描出および保存ができるようになった。さらに画像処理能力の向上により，3 次元画像をリアルタイムに表示できるようになり，リアルタイム 3 次元超音波（4D-US）が可能となった[3]。

c. 造影 4D-US

4D-US はすでに造影剤を用いることも可能となっている。初期にはドップラー画像よりレンダリングした 3D 画像を B モードよりレンダリングした 3D 画像と融合させることにより，組織内の血流を 3D 表示していたが，レボビストの登場により造影 3 次元超音波が可能となった。さらに，ソナゾイドの開発およびこれに対応した低音圧を用いた造影超音波モードが開発され，レボビストに比較して高いフレームレートで観察でき，実時間性が大きく向上した。すなわち，ソナゾイドの登場により，造影 4D-US においては，高いフレームレートから得られる連続断層画像を高い処理能力でレンダリングすることができるようになり，高いボリュームレートで画像の描出と保存が自動的にできるようになった。また，レボビストのようにマイクロバブルを壊すことなく超音波検査を行えるため，造影超音波のためのデータが大幅に増加し，空間分解能も向上した。

Ⅱ．方　法

超音波診断造影は Aplio XG（東芝メディカルシステムズ）を用いた。4D-US のボリュームレートは 0.3～5 vps とした。周波数は B モードは 5 MHz，造影モードは 3.5 MHz で行った。超音波造影剤はソナゾイドを用い，造影超音波のときは MI 値を 0.20～0.30 とした。